IOP Publishing Journal of Micromechanics and Microengineering
J. Micromech. Microeng. **26** (2016) 124004 (12pp) doi:10.1088/0960-1317/26/12/124004

A batch-fabricated electret-biased wideband MEMS vibration energy harvester with frequency-up conversion behavior powering a UHF wireless sensor node

Y Lu[1], E O'Riordan[2], F Cottone[1,5], S Boisseau[3], D Galayko[4], E Blokhina[2], F Marty[1] and P Basset[1]

[1] Université Paris-Est/ESYCOM/ESIEE Paris, Noisy-le-Grand, France
[2] University College Dublin, Dublin, Ireland
[3] CEA-LETI, Grenoble, France
[4] UPMC-Sorbonne Universités/LIP6, CNRS, Paris, France

E-mail: p.basset@esiee.fr

Received 15 March 2016, revised 23 April 2016
Accepted for publication 6 May 2016
Published 29 September 2016

Abstract

This paper reports a batch-fabricated, low-frequency and wideband MEMS electrostatic vibration energy harvester (e-VEH), which implements corona-charged vertical electrets and nonlinear elastic stoppers. A numeric model is used to perform parametric study, where we observe a wideband bi-modality resulting from nonlinearity. The nonlinear stoppers improve the bandwidth and induce a frequency-up feature at low frequencies. When the e-VEH works with a bias of 45 V, the power reaches a maximum value of 6.6 μW at 428 Hz and 2.0 g_{rms}, and is above 1 μW at 50 Hz. When the frequency drops below 60 Hz, a 'frequency-up' conversion behavior is observed with peaks of power at 34 Hz and 52 Hz. The −3 dB bandwidth is more than 60% of its central frequency, both including and excluding the hysteresis introduced by the nonlinear stoppers. We also perform experiments with wideband Gaussian noise. The device is eventually tested with an RF data transmission setup, where a communication node with an internal temperature sensor is powered. Every 2 min, a data transmission at 868 MHz is performed by the sensor node supplied by the e-VEH, and received at a distance of up to 15 m.

Keywords: electrostatic vibration energy harvester, electret-biased, nonlinear, wireless sensor node

(Some figures may appear in colour only in the online journal)

1. Introduction

Low frequency vibrations widely exist all over the environment, and are typically featured with large frequency bandwidths. Among them are mechanical vibrations, such as those of engines and machines, which are considered to be among the most promising sources for energy harvesting. The power of the these vibrations is distributed in the frequency band between 50 Hz and a few hundred hertz. However, low-frequency vibration energy collected by MEMS-based devices is still far from satisfactory. As stated in [1], the theoretical maximum power that can be collected by a resonant structure is related to its proof mass and maximum displacement. The miniature size of MEMS harvesters confines both these parameters, and the consequence is a low output power [2–4]. It can be desirable to reduce the spring stiffness so as to reduce the resonance frequency [5–7], but this technique might reduce the reliability of the structure. An alternative to improve the performance is to enlarge the operating frequency

[5] Now at University of Perugia, NIPS Laboratory, Department of Physics and Geology, Italy.

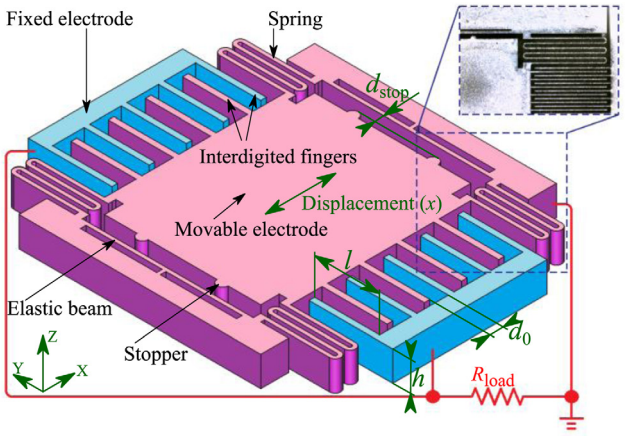

Figure 1. Simplified schematic of the silicon layer of the e-VEH. The nonlinear spring system consists of linear serpentine springs and non-linear elastic beams standing against stoppers. The image on the right upper corner is a microscopic photograph of the silicon structure.

bandwidth. One method is to use non-resonant structures without springs [8, 9] so that the working frequency can be greatly reduced, but without resonance we can no longer benefit from mechanical amplification of amplitude. A second way is to introduce nonlinearity such as bi-stability [10, 11] or piecewise stiffness of springs [12, 13], so that the frequency response will be expanded by hysteresis. However, the practical use of this bandwidth increase is still limited because of the existence of the low branch of the hysteresis, and because of difficulty to actively select the desirable (high) branch. Another way is to introduce impact as a strong nonlinear component in a resonant structure, realizing a frequency up-conversion structure [14–16].

In this work, we study a low-frequency wideband MEMS e-VEH in which linear springs and nonlinear stoppers are combined in a single-layered silicon structure to obtain frequency-up conversion behavior at low frequency and Duffing nonlinearities at high frequencies. A full batch process is used. The prototype is self-biased by a corona-charged vertical electret layer, and efficiently converts energy over all over the frequency range of 33–428 Hz.

In section 2, we describe the working principle of the proposed prototype and its fabrication. Then we analyze the impact of several parameters on the device performance in section 3 by modeling its behavior. In section 4, we introduce the characterization of the device, including the capacitance measurement, built-in voltage characterization, load analysis, tests on energy conversion performance with frequency sweeps, and with wideband noisy input. Finally, we validate that the proposed prototype can power one data transmission of a wireless UHF sensor node in every 2 min, delivering 155 μJ.

2. Device description and fabrication

The cardinal component of the MEMS e-VEH is a single-layered silicon structure, which is shown in figure 1. The central part of the structure is a movable silicon mass

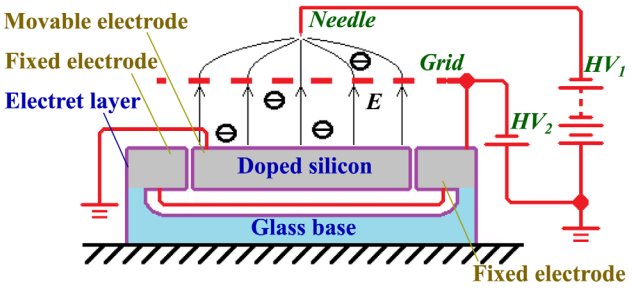

Figure 2. Schematic of the experimental set-up for the corona charging of the electret layer.

connected to fixed ends by linear serpentine springs. On the two ends of the device, there are elastic stoppers consisting of elastic beams on the fixed ends and semi-cylindrical protrusions on the movable mass [17]. Along the two sides of the device are gap-closing interdigited combs forming a variable capacitance. A thin layer of electret covers the entire surface of the device, and the device is internally biased by charges embedded in the electret layer only on the movable electrode. When the device is shaken with an acceleration above a certain amplitude, the displacement of the mass is so large that the protrusions will hit the elastic beams and bend them, resulting in a larger total stiffness of springs. These elastic stoppers introduce nonlinearity to the system and expand the bandwidth both at low and high frequencies.

The fabrication of the device, derived from [18], is quite simple. A bulk silicon wafer is firstly patterned with an aluminum mask by deep reactive-ion etching process on both sides, and anodically bonded with a glass handle wafer. Then, a layer of parylene-C is deposited by chemical vapor deposition all over the device. The device is put into a point-grid-plane corona-charging process where only the electret on the central electrode is charged negatively, as shown in figure 2. In order to ensure the selectivity of corona charging, the movable electrode is connected to the ground, while its counter electrode is connected to the grid voltage. The device is charged for 30 min with a point voltage of 13 kV and a grid voltage of 100 V. Pull-in between the electrodes occurs during the charging process. 24 h after the charging, the device is released due to the decay of the electret surface potential. After 3 weeks, the voltage on the electret becomes stable, so that we can perform experiments to characterize the device, and measure the real harvested power.

3. Device modeling and parametric study

3.1. Description of the numerical model

E-VEH devices require both a mechanical input (an external vibration) and an electrical input (an electret bias or an external DC bias voltage). Therefore the coupled force due to both mechanical and electrical domains needs to be considered simultaneously. This electrostatic force is given by the equation [19]:

$$F_e(x,q) = \frac{1}{2}\frac{q^2}{C_{var}(x)^2}\frac{dC_{var}(x)}{dx} \quad (1)$$

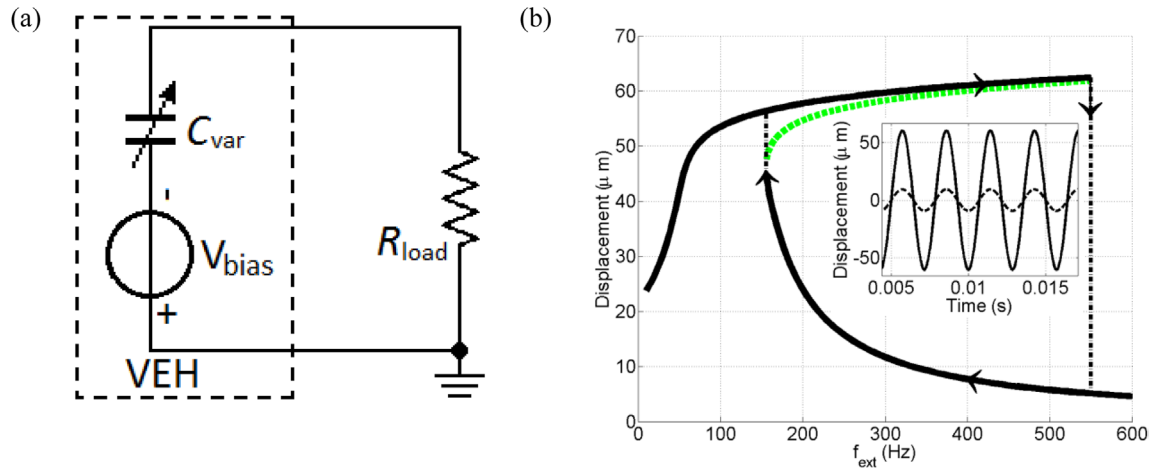

Figure 3. (a) The electrical model of the device and the conditioning circuit considered in the simulation of energy conversion (b) Frequency sweep of the resonator displacement at 2.0 g_{rms}, for $V_{bias} = 20$ V and $R_{load} = 6.65$ MΩ. Stable roots are shown with the full black and an unstable branch with a green dotted line. For experimental reference, the dot-dash lines show the corresponding up and down sweeps, with arrows. The inset shows the transient waveforms of the mass displacement of the two stable branches with the frequency of 350 Hz.

where x stands for the mobile mass displacement, q is the charge through the circuit and $C_{var}(x)$ is defined by the variable capacitors geometry. The device used in this study is characterized in section 4.1. The electrostatic force (1) is a nonlinear force which plays a fundamental role in the description and optimization of e-VEHs.

A simple electrostatic harvester consists of a second order resonator, a variable capacitor (transducer) C_{var}, and a conditioning circuit. For a sinusoidal external excitation (a_{ext}), the mobile mass displacement (x) in the mechanical domain, is described by the Newtonian equation:

$$\ddot{x} + \left(\frac{b}{m}\right)\dot{x} + (2\pi f_0)^2 x = a_{ext} + \frac{F_e(x,q)}{m} + \frac{F_{stop}(x)}{m} \quad (2)$$

where m is the mass of the resonator, b is the damping factor, f_0 is the natural frequency and F_{stop} stands for the force generated by the stoppers. The electrostatic force F_e describes the electrical transduction of energy from the mechanical domain. The importance of the electrostatic force can be seen if, for example, an external driving frequency near resonance is applied to the device. Increasing the bias voltage (V_{bias}) will ultimately cause the harvested energy to decrease This effect is due to a shift in the resonance frequency caused by the electromechanical coupling [20]. Such a decrease in power would not occur if a fixed $C_{var}(x)$ function was used (as is the case of purely electrical analysis when ignoring F_e).

Using Kirchhoff's voltage law, the circuit in figure 3(a) is simply described by:

$$R_{load}\dot{q} + \frac{q}{C_{var}(x)} = V_{bias} \quad (3)$$

where R_{load} is the load resistance and V_{bias} the bias voltage. Note the dependence of (3) on the resonator displacement x, highlighting the electromechanical coupling in the system (1)–(3).

The force of the stoppers is a strong nonlinear force due to its piecewise nature. It can be described as:

$$F_{stop}(x) = \begin{cases} -k_{stop}(|x| - d_{stop})\text{sign}(x), & |x| \geqslant d_{stop} \\ 0, & |x| < d_{stop} \end{cases} \quad (4)$$

where k_{stop} is the total stiffness of the elastic beams on either fixed end and d_{stop} is the position of the undeformed stopper's beam. Nonlinear stoppers along with the electrostatic force are used to enlarge the operating bandwidth and increase power yield. The system of nonlinear ordinary differential equations (1)–(4) is the primary model of this device. However due to the substantial nonlinear behavior it is helpful to employ semi-analytical methods, such as perturbation techniques, to obtain greater understanding of the device dynamics.

3.2. Semi-analytic techniques—multiple scales method

The multiple scales method (MSM) approaches the e-VEH as a simple resonator with a perturbation term. It then solves this by introducing different time scales [21].

A requirement of the presented method is that the electrostatic force F_e should be periodic. Thus the electrostatic force can be represented by a Fourier series. To achieve this, the forced displacement in the resonator is considered to be of the form $x_0\cos(\omega t + \varphi)$, where $\omega = 2\pi f_{ext}$. When applying the perturbation technique, it is advantageous that the resonator be relatively high Q, which is the case for this device. This allows the resonator to be thought of as a selective filter and so the nonlinear forces can be described by a Fourier series:

$$F = F_0 + a_1(a)\cos(\omega t + \varphi) + b_1(a)\sin(\omega t + \varphi) \quad (5)$$

where F_0, $a_1(a_0)$ and $b_1(a_0)$ are the coefficients of the Fourier series, $a = x/d$ and F represents a nonlinear force. Higher order terms can be included but, as the system is relatively high Q, their response is significantly smaller and so are ignored in this analysis. Calculating the Fourier series, the nonlinear forces are separated into their potential and dissipative components, respectively:

Table 1. Parameters of the model used in figures 3, 4, 8 and 10.

Proof mass (m)	59×10^{-6} kg
No. of fingers (N)	100
Finger length (l)	1.97×10^{-3} m
Finger thickness (h)	380 μm
Initial gap (d_0)	70 μm
Area (S)	7.486×10^{-5} m^2
Spring constant (k)	27.8 N $\cdot$ m^{-1}
Stopper spring constant (k_{stop})	8.64×10^3 N $\cdot$ m^{-1}
Position of the undeformed stopper's beam (d_{stop}) (estimated, used in figures 3, 4)	51 μm
Quality factor ($Q = \frac{\sqrt{m/k}}{b}$) (estimated, used in figures 3, 4)	6.5
Parasitic capacitance of the measurement set-up (measured, used in figures 8, 10)	28 pF

$$\begin{cases} a_1(a) = \dfrac{1}{\pi}\displaystyle\int_0^{2\pi} F\cos(\theta)\mathrm{d}\theta \\ b_1(a) = \dfrac{1}{\pi}\displaystyle\int_0^{2\pi} F\sin(\theta)\mathrm{d}\theta \end{cases} \tag{6}$$

where $\theta = \omega t + \varphi$. Further justification of the validity of the MSM for the analysis of e-VEH is provided in [22].

To apply the method, the electrical equation is generalized as a linear nonhomogeneous equation. The resulting MSM equation provides a solution for the steady-state amplitude of oscillations x_0, as a function of the Fourier terms $(a_1(a_0), b_1(a_0))$ and dimensionless parameters, where $a_0 = x_0/d$, $\alpha = A_{\text{ext}}/d(2\pi f_0)^2$, $\beta = b/4\pi m f_0$ and $\sigma = ((2\pi f_{\text{ext}}/\omega_0) - 1)$:

$$\frac{\alpha^2}{4} = \left(a_0\sigma + \frac{a_1(a_0)}{2}\right)^2 + \left(a_0\beta + \frac{b_1(a_0)}{2}\right)^2. \tag{7}$$

Solving this for a_0, the steady-state solution of x can be determined in the form:

$$x_0(t) = x_{\text{av},0} + a_0 d\cos\left(2\pi f_{\text{ext}} t + \theta_0 - \varphi_0\right). \tag{8}$$

Semi-analytic methods are not intended to replace experimental or numerical results, but rather to verify results or explain dynamics of the system. An additional benefit of semi-analytic approaches is the speed of simulations allowing multi-parameter analysis, for instance, for the optimization of power.

3.3. Optimization and multi-stability due to nonlinear stoppers

In this section we use the model presented above with the numeric parameters for the device in figure 1, in order to show the system's dynamic behavior and to determine a configuration (e.g. the load resistance and the bias voltage) maximizing the energy conversion. The solutions resulting from the model are discussed from the perspective of the experimental results given in section 4.4. The parameters used for this modelling are given in table 1. Some parameters are estimated from the geometry of the device with a high degree of confidence (e.g. the mass, the initial gap, the stiffness of the springs), and others are estimated indirectly. According to [23, 24], the damping effect of air thin film is greatly affected by the thickness of air film, and a linear damping model is only a rough approximation of real physical phenomena. The quality factor used in the model represents globally the losses experienced by the resonator during the vibrations. It is estimated to be 6.5, see table 1. We consider that the use of a simplified damping model is the main source of discrepancy between the experimental results and the modeling (see discussion on the comparison with the experiment in section 4.3). The used initial gap value corresponds to the approximated model of the transducer, which is justified in section 4.1, see equation (7). The total parasitic capacitance of the measurement set-up (28 pF) is another parameter not accounted for in the MSM model.

Both the electromechanical coupling (electrostatic force) and the mechanical stoppers, are important nonlinear forces determining the optimum power of the device. Bi-modality is one type of nonlinear behavior which is present in the proposed device. Bi-modality occurs when, for the same external excitation and circuit parameters, more than one stable mode exists. It means that the device may highlight two (or more) dynamic behaviors, for example, with different amplitudes. The actual mode in which the system is in at a given moment depends on the history, e.g. on the initial conditions. The existence of bi-modal behavior, due to the electrostatic force and stoppers, is shown in figure 3(b) (obtained by simulation) for 2.0 g_{rms} excitation (the subscript 'rms' means that the root mean square of excitation is 2.0 g, with $g = 9.8$ m $\cdot$ s^{-2}, same below), where for the frequency range 160–550 Hz, the device may vibrate with one of two possible amplitudes. The benefit of an analytical approach, such as the MSM, is that it directly shows all modes. Without the nonlinear electrostatic force and stoppers, there is only one root of (5). Thus the bi-modal behavior can only be caused by the nonlinear terms. This behavior of Duffing oscillators is widely discussed in the literature [25–28]. The two modes correspond to two different forced vibrations in the resonator, one with large amplitude and the other with smaller amplitude. This is shown in the inset of figure 3(b). Of course, beyond certain physical limit, the system can experience pull-in and the movable electrode will enter into an unrealistic regime and be stuck to one end.

In order to give an example of the use of the presented model for the system design optimization, figure 4 presents two parametric planes representing the energy generated by the harvester on the load resistance during one period of mechanical vibrations. The two planes are obtained for fixed amplitude and frequency of input vibrations, 0.5 g_{rms} and 2.0 g_{rms}, the same parameters as in the experiment in section 4.4. It can be seen that in both cases there is an optimal set of $(R_{\text{load}}, V_{\text{bias}})$ maximizing the energy yield.

4. Device characterization

The performance of the device was characterized by a series of experiments described in this section as discussed below. In controlling the acceleration of the shaker (V400 series vibrator from Brüel & Kjær) carrying the MEMS e-VEH,

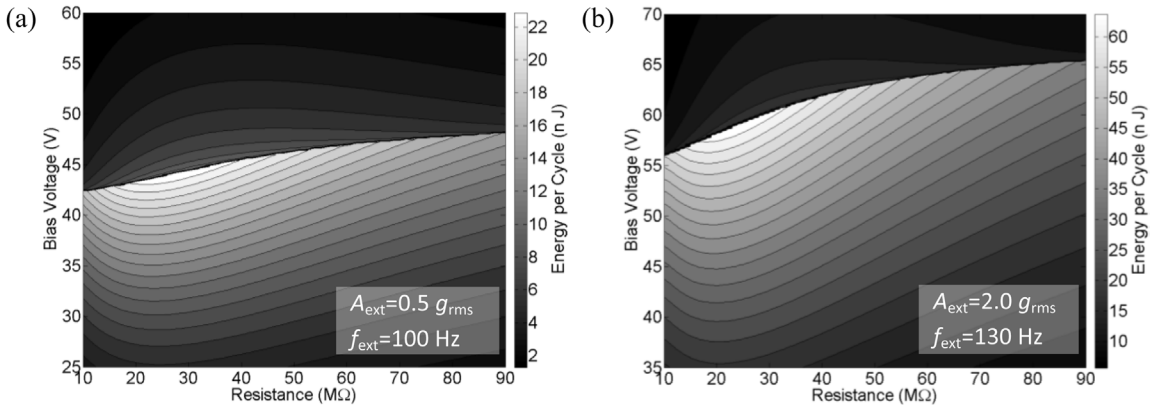

Figure 4. Power plane showing a local maximum in the power at (a) 0.5 g_{rms} input acceleration at 100 Hz and (b) 2.0 g_{rms} input acceleration with a driving frequency of 130 Hz.

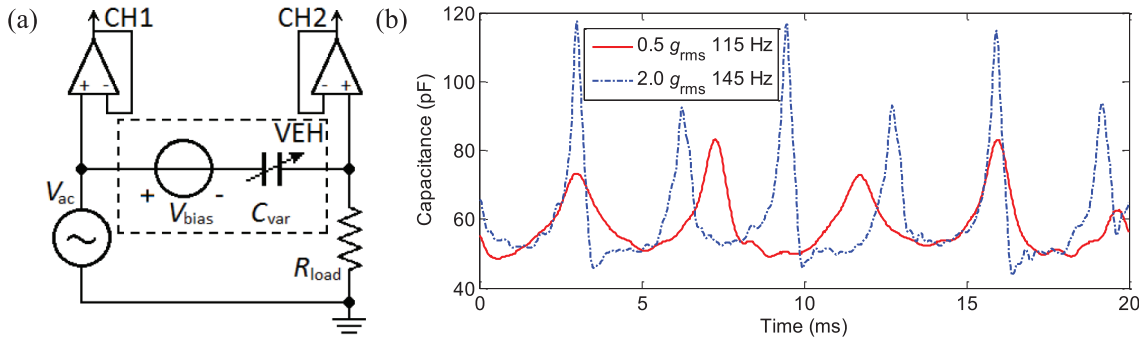

Figure 5. (a). Schematic for the measurement of capacitance, (b) capacitance variation at acceleration of 0.5 and 2.0 g_{rms}, including a 28 pF parasitic capacitance.

we attach an accelerometer (Type 4507 B 004 of DeltaTron) to the harvester so as to realize a close loop control. According to the requirement of measurement, we generate arbitrary controlling signals including single-frequency signals, signals sweeping through a range of frequencies with a uniform amplitude, etc.

4.1. Capacitance variation

Theoretically, the displacement-capacitance function $C_{var}(x)$ is that of a symmetrical gap closing transducer:

$$C_{var}(x) = \varepsilon_0 \frac{2Sd_0}{d_0^2 - x^2} \tag{9}$$

where S is the overlapping area of the electrodes, d_0 is the initial gap between electrodes, ε_0 is the permittivity of the vacuum. Hence, if the displacement is sinusoidal with amplitude X_0, the extreme values of the capacitances during the device deformation are given by:

$$C_{min} = \varepsilon_0 \frac{2Sd_0}{d_0^2}, C_{max} = \varepsilon_0 \frac{2Sd_0}{d_0^2 - X_0^2}. \tag{10}$$

It can be seen that the minimum capacitance is only defined by the device geometry, whereas the maximum value is a function of the amplitude X_0. In practice, the maximum/minimum capacitance is affected by several factors: fabrication tolerances (actual value of the initial gap, non-verticality of the transducer wall due to the under-etching [18]), the presence of the parylene layer on the electrodes and the importance of the electrostatic force. Moreover, it is difficult to know the real amplitude X_0. Hence, the characterization of the capacitance variation is an important step described in this section.

The schematic of the capacitance measurement is shown in figure 5(a), where an AC signal V_{ac} is applied to the device in series with a resistor R_{load}. By detecting the phase difference of the signals on the two nodes of the device (i.e. signals CH1 and CH2 in figure 5(a)), its capacitance can be measured dynamically [30]. In order to minimize the error of the measurement, the value of the load should be the optimal value given by:

$$R_{opt} = (\omega \overline{C})^{-1} \tag{11}$$

where ω stands for the angular frequency of the carrier signal V_{ac}, and $\overline{C}$ is the average value of the device's capacitance. To choose the optimal load, we firstly employ the capacitance variation range given by simulation, and use the estimated optimal load for a rough measurement. The result of this test is then used for recalculating the optimal load, and the capacitance is re-measured using the new optimal load. In the experiment we apply a sinusoidal carrier (V_{ac}) with the frequency of 50 kHz and the peak–peak amplitude of 2 V, while the load resistance is 53 kΩ. The operational amplifier used is OPA445AP from Texas Instruments (same below). The capacitance variations at 0.5 and 2.0 g_{rms} are shown in figure 5(b).

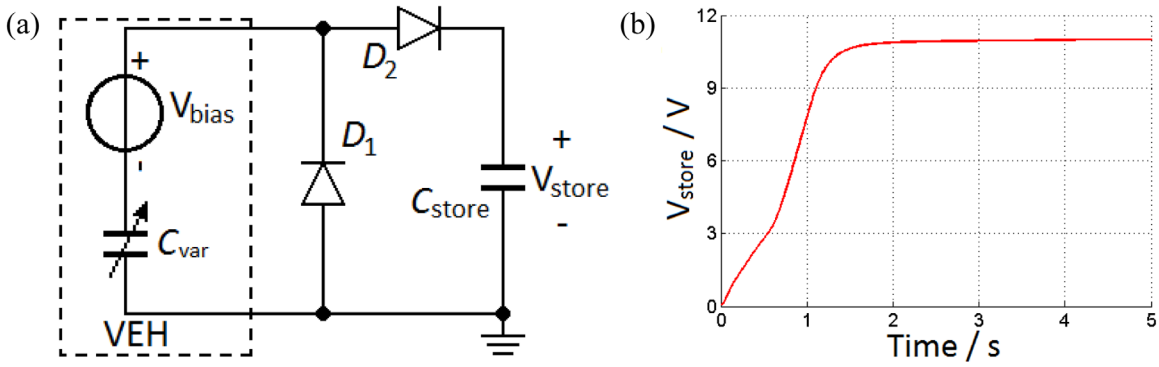

Figure 6. (a) Schematic for the built-in voltage measurement of the electret layer, (b) measure of the evolution of V_{store} at 2.0 g_{rms}, 145 Hz, where $C_{\text{store}} = 1.1$ nF.

It is observed that in each period of mechanical vibration, there are 2 peaks in the capacitance evolution, corresponding to the maximum displacement of the movable electrode in 2 directions. This is explained by the fact that the function $C_{\text{var}}(x)$ is even (due to the symmetric geometry of gap-closing combs), see equation (9). There is an obvious difference between the values of the 2 peaks, indicating an asymmetric oscillation of the movable electrode. The increase of acceleration introduces an enlarged range of capacitance variation, where the peak values increase and the minimum remains almost the same: for the acceleration of 0.5 g_{rms} the range of capacitance is 50–80 pF and the average peak value is 78 pF, while for 2.0 g_{rms} the capacitance varies from 48 pF to 115 pF with the average peak value of 105 pF. These values include a parasitic capacitance of 28 pF induced by the measurement setup.

4.2. Built-in voltage

After the corona-charging, when the charge in the electret becomes stable (after 3 weeks), the built-in voltage of the device (V_{bias}) provided by the electret was measured using the circuit shown in figure 6(a). The output current of the device was connected to a storage capacitor C_{store} through a half-wave diode bridge rectifier. This circuit corresponds to a rectangular QV cycle during the cycle of capacitance variation [19, 20], in which the converted energy in each cycle is given by the equation:

$$\Delta W = (V_2 - V_1)(Q_2 - Q_1) \tag{12}$$

where V_1 and V_2 stand for the extreme voltages on the capacitor C_{var}, while Q_1 and Q_2 are the extreme values of transducer charge Q_{var}. Note that the quantity Q_{var} represents the charge on the capacitor in the equivalent model of the transducer in figures 3(a) and 5(a), and not the distribution of the physical charges on the capacitor planes. However, the derivative of Q_{var} represents the physical current through the device. These extreme values are given by the following equations,

$$\begin{cases} V_1 = V_{\text{bias}} - V_{\text{store}}; & V_2 = V_{\text{bias}} \\ Q_1 = V_1 C_{\max}; & Q_2 = V_2 C_{\min} \end{cases} \tag{13}$$

where V_{store} is the voltage on the storage capacitor, while $C_{\min}$ and $C_{\max}$ are the extreme values of the device's capacitance.

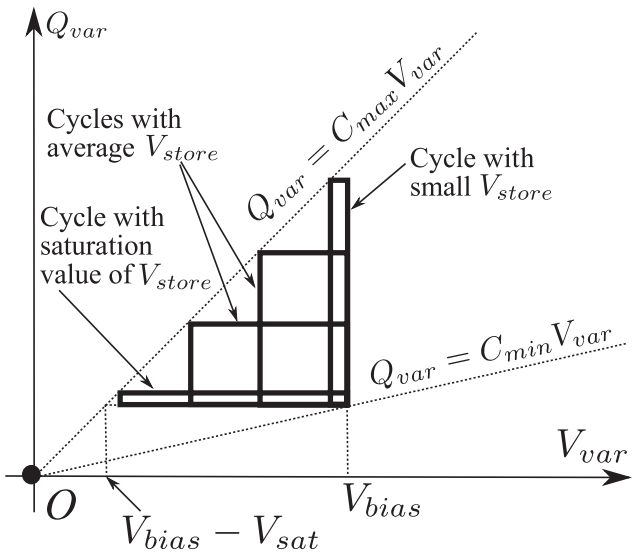

Figure 7. QV cycles of the half wave rectifier used with a variable capacitor biased by an electret.

The QV cycles achievable with different values of V_{store} are represented in figure 7.

Because of the capacitance variation, the voltage across C_{store} increases and finishes by being saturated. Simple calculation highlights a relation between the measured saturation voltage V_{sat} and the built-in voltage V_{bias}.

By merging equations (12) and (13), we can derive that:

$$\Delta W = V_{\text{bias}} V_{\text{store}} C_{\max}(1 - V_{\text{store}}/V_{\text{bias}} - C_{\min}/C_{\max}). \tag{14}$$

To ensure non-negative energy conversion, the following relation must be held:

$$V_{\text{store}}/V_{\text{bias}} \leqslant 1 - C_{\min}/C_{\max} \tag{15}$$

so that the maximum allowed V_{store} is the saturation voltage V_{sat}, which is given by:

$$V_{\text{sat}} = V_{\text{bias}}(1 - C_{\min}/C_{\max}). \tag{16}$$

Thus the bias voltage of the device is indicated by the saturation voltage if the ratio of maximum and minimum capacitance is known:

$$V_{\text{bias}} = \frac{V_{\text{sat}}}{1 - C_{\min}/C_{\max}}. \tag{17}$$

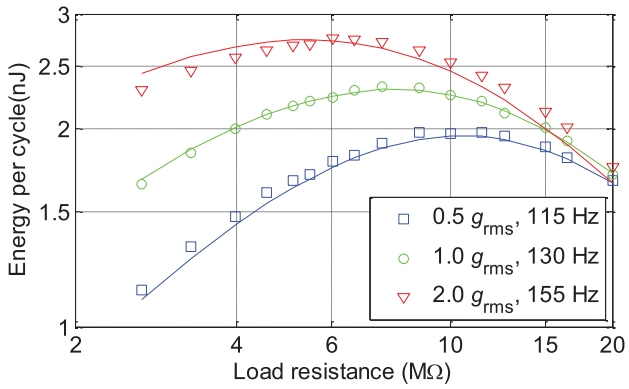

Figure 8. Influence of the load resistance on the converted energy in each cycle of mechanical vibration with various amplitudes of acceleration. The device is biased only by the electret at 20 V and is shaken at the frequency that offers maximum capacitance variation. The symbols are experimental results, and the plain lines are the results given by the model of section 3.1. solved numerically (the parameters applied are described in section 4.4).

Note that the polarity of the connection of the electret bias matters: for an inverse polarity of V_{bias} in figure 6(a), the expression for the saturation voltage and the aspect of the QV cycles are different [29].

In the experiment, the device was submitted to vibrations with acceleration of 2 g_{rms} and 145 Hz, and the measured saturation voltage is 11.5 V, as shown in figure 6(b). Considering that the capacitance is comprised between 48 pF and the peak value of 115 pF, we can infer that the bias voltage of the electret is 20 V. Since the device can withstand higher bias voltages, we have also applied an external bias in addition to the internal one in some of the following experiments. The limit for the bias voltage is 45 V, and above this value we observe dynamic pull-in between electrodes during the experiment.

4.3. Optimal load resistance analysis

The output power of the device was tested with a varying load resistance (see figure 1 for the circuit), so that the optimal matching load could be found for each amplitude of acceleration. The chosen frequency of vibration for each amplitude was the one that provided the maximum variation of capacitance. In these measurements, the device was biased only by the internal voltage of the electret (20 V). Shown in figure 8 are the energy consumptions of the sweeping load resistance at different accelerations. As stated in [18], the load resistance affects the QV cycle in two major aspects: with a large resistance the charge variation is limited, while with a small load the voltage is nearly constant, resulting in limited power in both cases. So we can obtain a medium optimal load resistance corresponding to an optimal energy conversion cycle.

We observe a decreased optimal load (R_{opt}) with increased acceleration, which is similar to the observation in [31]: R_{opt} for 2.0 g_{rms} is 6 MΩ, and is 10 MΩ for 0.5 g_{rms}. This can be explained as a result of the nonlinearity in the system. We also notice that with the increase of the load resistance, the increase of energy conversion in each QV cycle, due to the increase of the acceleration, is less evident. This can be explained as follows. The increase of the load resistance results in an enlargement of the variation of the voltage. Consequently, when the amplitude of the mass motion is large, so that the gap becomes very small at extreme positions of the mobile electrode, the electrostatic force increases significantly (inversely proportional to the square of the gap). This creates a mechanism further reducing the gap, and in turn enlarging the capacitance variation range and the voltage variation. Thanks to this positive feedback mechanism, the increase of maximum displacement with increased acceleration at large R_{load} is less prominent, so is the increase of power.

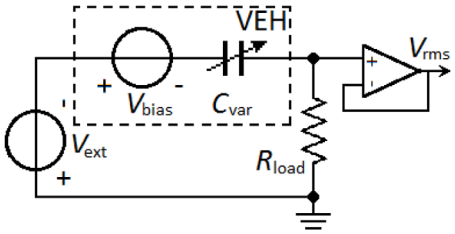

Figure 9. Schematic for the measurement of converted energy as a function of the DC bias.

4.4. Performance with frequency sweeps

In the experiments in this section and the following one, the device was loaded by a resistor of 6.65 MΩ. We varied the bias of the device by either merely using the internal bias of the electret ($V_{bias} = 20$ V) as shown in figure 1, or applying an additional external DC voltage ($V_{ext} = 25$ V) in addition as shown in figure 9. Thus the maximum allowed bias voltage was attained, so that we could have a knowledge about the maximum energy conversion of the device, as stated in section 4.2. The energy of the voltage source V_{ext} was only spent to initially bias the device, and during the energy conversion, the average power delivered by the source is zero.

The device was shaken through frequency sweeps with various amplitudes of acceleration. The output power is given by the rms voltage (V_{rms}) on R_{load}. With a 0.1 g_{rms} acceleration, the peak power is achieved at the natural frequency $f_0 = 104$ Hz. Shown in figure 10 are the converted energy in each cycle of the external mechanical vibration at higher accelerations (0.5 and 2.0 g_{rms}), which is obtained by dividing the output power with the mechanical vibration frequency. We observe a hysteresis due to spring-hardening effect of the nonlinear stoppers, which reinforces the bi-modal behavior predicted by the numerical model (see section 3.3). The frequency range of this spring-hardening hysteresis is greatly increased under large accelerations, bringing great improvement to the bandwidth. At 2.0 g_{rms} with 45 V bias, the maximum −3 dB band is 223–432 Hz including hysteresis and 88–166 Hz when excluding it.

Unlike with the amplitude of external vibrations, increasing the bias voltage almost does not affect the bandwidth (only a 5% increase of bandwidth with the bias increased from 20 V to 45 V). However, the increased bias increases the electrostatic force between interdigited combs, resulting in a reduced

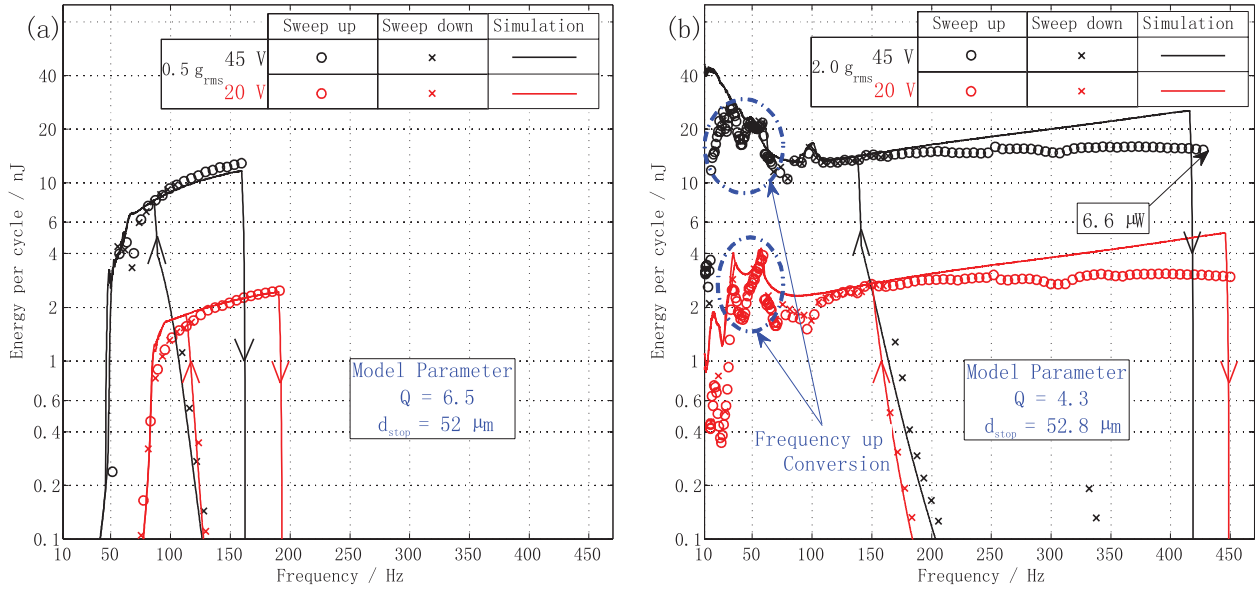

Figure 10. Energy converted in each cycle of mechanical vibration versus its frequency for bias voltages of 20 V (electret alone) and 45 V (electret @ 20 V + DC external bias @ 25 V) at 0.5 g_{rms} (a) and 2.0 g_{rms} (b), $R_{load} = 6.65$ MΩ. The circles and crosses correspond to the measurement with frequency sweeps, while the plain lines depict the prediction given by the model of section 3.1 solved numerically.

stiffness of the spring system (spring softening effect). The consequence is a shift towards low frequency in the frequency response of the device.

The maximum power that can be achieved at 2.0 g_{rms} is 6.6 μW. It is well established that the converted energy with a given capacitance variation cycle is proportional to the bias voltage squared, and increases with the enlargement of capacitance range [32]. As expected, we observe an approximately linear relationship between the output power and the square of the bias voltage, which suggests that with these parameters of external vibrations the range of capacitance variation is not sensitive with regard to the voltage. As mentioned in section 3.1, it means that the amplitude X_0 is less dependent on the bias voltage than on the mechanical factors.

However, there is an obvious increase of converted energy in each mechanical cycle at the acceleration of 2.0 g_{rms} within the frequency range of 30–60 Hz, instead of keeping a constant value as for higher frequencies. Within this range, there are 2 peaks at 52 Hz and 34 Hz, corresponding to 1/2 and 1/3 of f_0 respectively. This increase of energy is representative of a frequency-up conversion mechanism [14] induced by the elastic stoppers where there are several bounces of the movable mass in each period of external vibration. So that, there are several peaks of capacitance in each cycle of the carrier's vibration.

The behavior observed by the experiment in figure 10 is well reproduced by the analytical model presented in section 3.1, when the system of nonlinear equations (1)–(4) is solved by a numerical method, see figure 10, plain lines. In particular, frequency-up conversion behavior and the bimodality are well predicted. However, because of approximation in the model of the air damping (discussed in section 3.3), some model parameters need to be tuned for each value of external acceleration, for the numerical values predicted by the model coincide with the experimental results. The adjustment is done on two parameters Q (quality factor) and d_{stop} (position of the undeformed stopper's beam) as shown in table 2.

Table 2. Parameters of the analytical model of section 3.1 adjusted for matching with the experimental results given in figures 8 and 10.

Position of the undeformed stopper's beam (d_{stop})	52 μm (0.5 g_{rms})
	52.8 μm (1.0 g_{rms} & 2.0 g_{rms})
Quality factor (Q)	6.5 (0.5 g_{rms})
	5.4 (1.0 g_{rms})
	4.3 (2.0 g_{rms})

After this adjustment, the analytical model provides a frequency response very close to what was observed experimentally. One can conclude that the proposed model describes well the main features of the system dynamics, but is still unable to predict the exact numerical values of the dynamic parameters (amplitude, power) without a post-experiment model tuning. This is a serious shortcoming of the analytical and modeling techniques of e-VEH, which is mainly due to the absence of reliable and handful predictive models of the air damping at large motion amplitude.

In contrast with the analytical model solved by a numerical method, the frequency-up conversion at low frequencies is not predicted by the model based on the multiple scales method (section 3.2), see figure 3(b), because the used analytical model is configured to predict only the oscillations at the same frequency as the input excitation. A modification of the method should allow a correct description of the dynamic of the device in the whole frequency range. This is a subject of ongoing work.

4.5. Performance with wideband Gaussian noise

The device was excited under a wideband colored Gaussian noise (with the autocorrelation time of 1 ms). Figure 11 shows

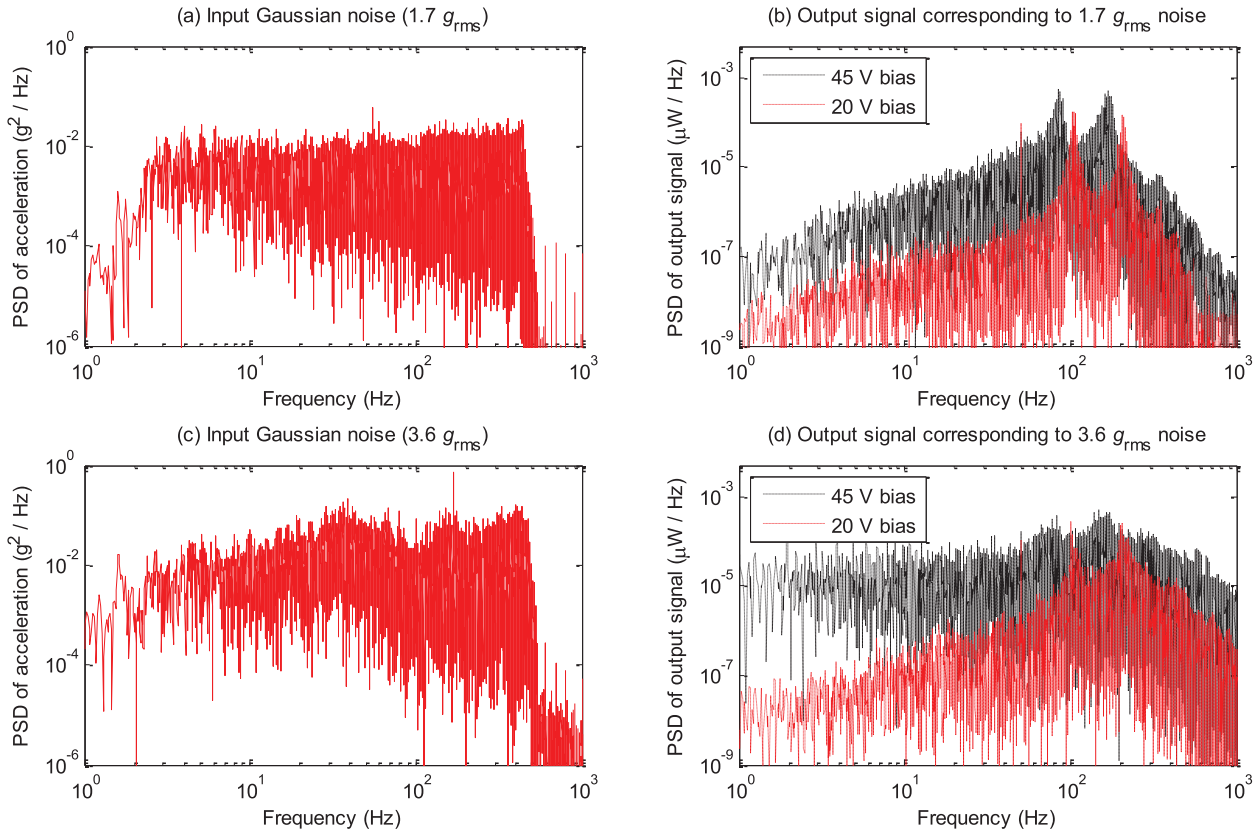

Figure 11. The PSD of the device output (b) and (d) to Gaussian noises with the acceleration of amplitudes 1.7 g_{rms} (a) and 3.6 g_{rms} (c) respectively, with varied bias voltage.

the Power-Spectrum Density (PSD) of the input and output signals. The input signals are distributed within the frequency range of 2–450 Hz, and the power density of acceleration throughout the bandwidth is in the order of 10^{-2} $g^2 \cdot Hz^{-1}$. These inputs are featured with Gaussian distributions with zero means and standard deviations of 1.7 g_{rms} and 3.6 g_{rms} respectively. The PSD functions are acquired according to the FFT spectrum of transient signals.

We can clearly see 2 major components in the PSD of the output signal. With 20 V bias and 1.7 g_{rms} input, the major components of output are 104 Hz and 208 Hz, which are the device's natural frequency and the second harmonic of the resonance respectively. The second harmonic is caused by the capacitance variation frequency doubling induced by the gap-closing interdigitated comb geometry [18]. The peak at the resonance frequency is related to an asymmetric vibration of the movable mass. With the bias of 45 V, these 2 peaks are shifted to lower frequencies of 85 Hz and 170 Hz, which is caused by the spring-softening effect of the electrostatic force. The peaks are more 'rounded' with higher acceleration and higher bias voltage. A flattening of the output power PSD at high bias voltage and at high input vibration amplitude may be explained by frequent collisions on the stoppers. The force field near maximum displacement is complex: it is a superposition of the forces generated by the linear springs, the elastic beams, the air damping and the deep electrostatic potential well near the transducer electrodes. In such a configuration, it is likely that collisions on the stoppers, at high kinetic energy, may lead to chaotic behavior. Chaos produces a dithering effect: the energy of the narrow frequency bands is distributed over a large band.

With an increased rms of the Gaussian acceleration, the output power PSD is increased over the entire spectrum, while the peaks of the output voltage PSD stay approximately at the same position, only a few hertz lower. The peaks of the PSD are not as prominent as with the lower acceleration. Taking the bias of 20 V for example, the level of the 'valley' in the PSD observed between the 2 peaks is 22% of the peak values with the acceleration of 3.6 g_{rms}, while the value for 1.7 g_{rms} is only 10%. This indicates a growth of bandwidth with increased acceleration, which can be explained by the effect of the non-linearity in the system.

By comparing the output PSD under the same excitations with different bias, we also note an obvious enhancement of power with high bias voltages, especially at low frequencies, which is consistent with the frequency sweep measurements (figure 10). An impressive enhancement of the PSD at low frequency for high bias voltage and high amplitude of external vibrations is observed, see the 45 V curve in figure 11(d). This can be explained by the dithering effect mentioned above. Despite of a reduced PSD of the input vibrations at low frequencies, see figure 11(c), the observed output PSD is close to flat over a broad frequency range, approximately from 1 to 200 Hz.

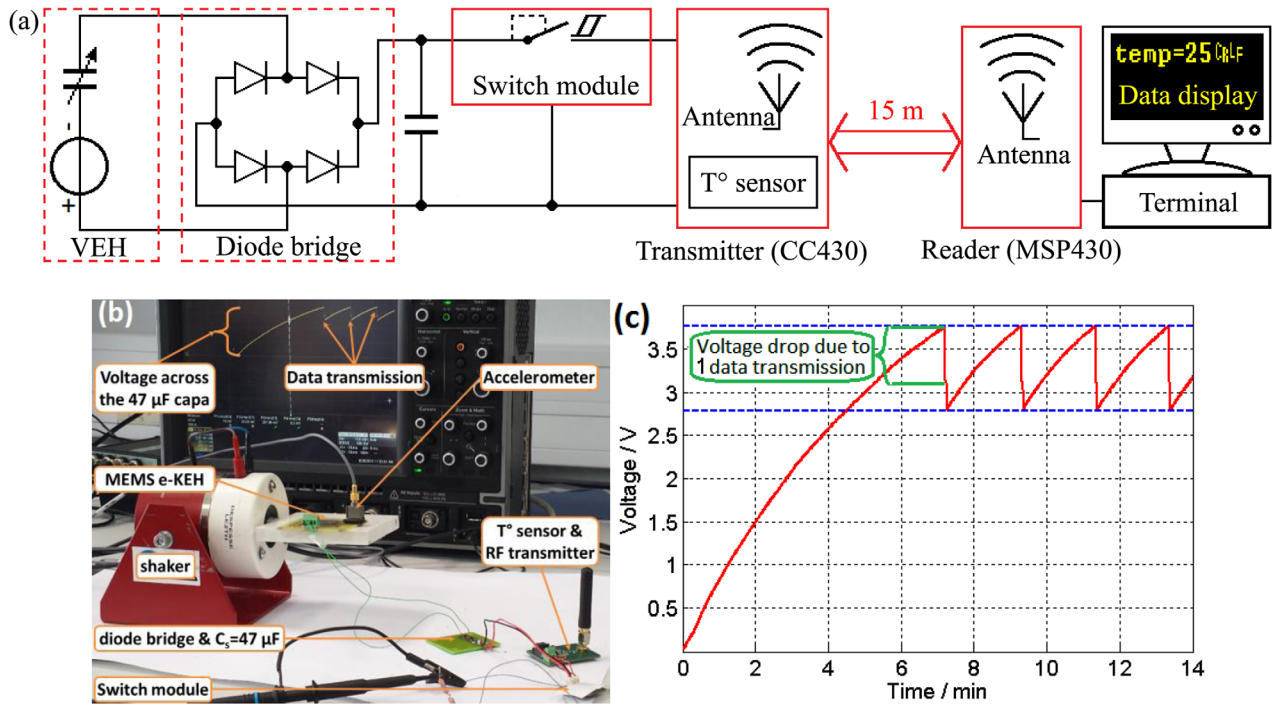

Figure 12. (a) Schematic and (b) photograph of the experiment of data transmission; (c) voltage evolution on C_{store} with time during the experiment.

4.6. Data transmission experiment

The device was then tested with a data transmission experimental setup, as shown in figures 12(a) and (b). In order to generate a DC load supply, the load resistance in figure 1 was replaced by a diode bridge, which was connected to a 47 μF storage capacitor C_{store}. A low-power Schmitt trigger (switch module) was connected to the storage capacitor to control the release of energy to a wireless sensor node (CC430). The operation of the switch is automatically controlled by its input voltage: the turn-on event takes place when the input voltage reaches 3.8 V, while the turning off occurs when the voltage drops to 2.8 V. Thus, unnecessary discharge of the storage capacitor can be prevented, and the voltage on the capacitor will be kept within the range of 2.8–3.8 V after the 1st charging. The current consumption of this switch module is lower than 40 nA (only 10% of the consumption of a 10 MΩ oscilloscope probe). When the transmitter was working, the temperature sensor node was read by a microcontroller (MSP430), and its data was transferred at RF frequency of 868 MHz to a remote receiver at a distance up to 15 m.

Figure 12(c) shows the voltage evolution on the storage capacitor during the data transmission experiment where the device is shaken at 300 Hz and 2.0 g_{rms}. The initial charging from 0 to 3.8 V takes about 7.2 min, where the accumulated energy is 334 μJ, corresponding to an average harvested power of 0.77 μW. When the voltage V_{store} reaches 3.8 V, the Schmitt trigger turns on the switch (PMOS transistor) and the sensor node starts to work. The temperature is measured by the internal sensor integrated in the microcontroller, and the data is sent wirelessly by RF at 868 MHz. The power consumption for one full data transfer is 102 μJ, corresponding to a voltage drop of 0.7 V. Hereafter, V_{store} drops to 2.8 V, and the Schmitt trigger turns off the PMOS switch so that the capacitor C_{store} can be recharged until its voltage reaches 3.8 V again. The recharging process requires about 2 min, where 155 μJ is collected, while the average power is now 1.27 μW. Then a new measurement cycle is performed.

5. Conclusion

We have reported a batch-fabricated low frequency and wideband MEMS e-VEH with corona-charged vertical electret and nonlinear elastic stoppers. The device is internally biased by the pre-charged electret, and thanks to the nonlinearity introduced by the stoppers, the bandwidth of the device's frequency response is greatly improved in both high and low frequency ranges.

In this study, we included an analytical and a numerical model of the presented prototype. A perturbation technique (Multiple Scales Method) was used. Its benefit is that it provides a straight insight into the nonlinear dynamics of the system, for instance the bimodality, for different control parameters, which is good for optimization of the system. With the numerical model, we can predict the frequency-up conversion behavior at low frequency, but the model needs to be improved at very low frequency. Moreover, both models predict the hysteresis at high frequency range. The main difficulty in the analytical study of the device is an uncertainty of the physical models, in particular, the air damping effects and the shape of the vertical walls in the structure.

For characterizing the prototype, we measured its capacitance variation through dynamic measurement, where we found the ratio C_{max}/C_{min} of 4.4 (2.4 when including the parasitic capacitance from the measurement set-up). This means

the device will work well with the Bennet's doubler conditioning circuit [33]. We also observe a difference between the 2 peak values of capacitance corresponding to each single cycle of mechanical vibration, which indicates the asymmetric displacement of the proof mass. In addition, the internal bias of the electret is characterized by a half-wave diode bridge charging a storage capacitor. The remaining voltage of the electret after 3 weeks is 20 V, which can still be improved to 45 V (the maximum allowed voltage of the device without dynamic pull-in) by optimizing the charging process and the materials (thermal treatments, coatings, …).

We also analyzed the optimal load with varied acceleration, and observed an optimal load resistance of 6–10 MΩ. The optimal load decreases with an increased acceleration, which can be explained as a result of nonlinearity. This decrease of optimal load agrees with the result given by the analytical model.

The measured power of energy conversion is 6.6 μW at 2.0 g_{rms} @ 428 Hz and 1 μW at 2.0 g_{rms} @ 50 Hz. Thus, a corresponding maximum power density of 132 $\mu\mathrm{W}\cdot\mathrm{cm}^{-3}$ is demonstrated. A large bandwidth is observed in the tests with frequency sweeps, which is majorly due to an over-all spring-hardening hysteresis introduced by the nonlinear forces. The −3 dB bandwidth with and without hysteresis are 210 Hz and 80 Hz respectively. An increase of power is observed at high acceleration around 50 Hz, which is caused by frequency up-conversion behavior due to multiple bouncing of the mobile mass on the elastic stoppers for a single mechanical oscillation. In a test with a colored wideband Gaussian noise activation, the output of the device contains 2 major frequency components related to the main system resonance and to the asymmetric vibration respectively. With larger bias voltage and larger acceleration, the output PSD is more uniform throughout the spectrum, which results from the more frequent occurrence of dithering due to the impact of stoppers.

The device is also tested with an energy management circuit to power a UHF wireless sensor node. A series of temperature measurements and data transmissions can be performed every 2 min, validating the whole energy harvesting chain. The average power in each recharging process is 1.27 μW, with the device shaken at 2.0 $g_{\mathrm{rms}}\cdot 300$ Hz.

References

[1] Mitcheson P D, Yeatman E M, Rao G K, Holmes A S and Green T C 2008 Energy harvesting from human and machine motion for wireless electronic devices *Proc. IEEE* **96** 1457–86

[2] Wang F and Hansen O 2014 Electrostatic energy harvesting device with out-of-the-plane gap closing scheme *Sensors Actuators* A **211** 131–7

[3] Liu H, Koh K H and Lee C 2014 Ultra-wide frequency broadening mechanism for micro-scale electromagnetic energy harvester *Appl. Phys. Lett.* **104** 053901

[4] Liu W, Han M D, Meng B, Sun X, Huang X and Zhang H 2014 Low frequency wide bandwidth MEMS energy harvester based on spiral-shaped PVDF cantilever *Sci. China Technol. Sci.* **57** 1068–72

[5] Naruse Y, Matsubara N, Mabuchi K, Izumi M and Honma K 2009 Electrostatic micro power generation from low-frequency vibration such as human motion *J. Micromech. Microeng.* **19** 094002

[6] Liu H, Lee C, Kobayashi T, Tay C J and Quan C 2012 A new S-shaped MEMS PZT cantilever for energy harvesting from low frequency vibrations below 30 Hz *Microsyst. Technol.* **18** 497–506

[7] Minakawa Y, Chen R and Suzuki Y 2013 X-shaped-spring enhanced MEMS electret generator for energy harvesting *2013 Transducers & Eurosensors XXVII: The 17th IEEE Int. Conf. on Solid-State Sensors, Actuators and Microsystems (TRANSDUCERS & EUROSENSORS XXVII)* pp 2241–4

[8] Yang B and Lee C 2010 Non-resonant electromagnetic wideband energy harvesting mechanism for low frequency vibrations *Microsyst. Technol.* **16** 961–6

[9] Lu Y, Wang X, Wu X, Qin J and Lu R 2014 A non-resonant, gravity-induced micro triboelectric harvester to collect kinetic energy from low-frequency jiggling movements of human limbs *J. Micromech. Microeng.* **24** 065010

[10] Le C P and Halvorsen E 2013 Wide tuning-range resonant-frequency control by combining electromechanical softening and hardening springs *2013 Transducers & Eurosensors XXVII: The 17th IEEE Int. Conf. on Solid-State Sensors, Actuators and Microsystems (TRANSDUCERS & EUROSENSORS XXVII)* pp 1352–5

[11] Nguyen S D, Halvorsen E and Paprotny I 2013 Bistable springs for wideband microelectromechanical energy harvesters *Appl. Phys. Lett.* **102** 023904

[12] Soliman M S M *et al* 2008 A wideband vibration-based energy harvester *J. Micromech. Microeng.* **18** 115021

[13] Suzuki Y, Miki D, Edamoto M and Honzumi M 2010 A MEMS electret generator with electrostatic levitation for vibration-driven energy-harvesting applications *J. Micromech. Microeng.* **20** 104002

[14] Galchev T, Aktakka E E and Najafi K 2012 A piezoelectric parametric frequency increased generator for harvesting low-frequency vibrations *J. Microelectromech. Syst.* **21** 1311–20

[15] Liu H, Tay C J, Quan C, Kobayashi T and Lee C 2011 Piezoelectric MEMS energy harvester for low-frequency vibrations with wideband operation range and steadily increased output power *J. Microelectromech. Syst.* **20** 1131–42

[16] Lu Y, Cottone F, Boisseau S, Marty F, Galayko D and Basset P 2015 A nonlinear MEMS electrostatic kinetic energy harvester for human-powered biomedical devices *Appl. Phys. Lett.* **107** 253902

[17] Lu Y, Cottone F, Boisseau S, Galayko D, Marty F and Basset P 2015 Low-frequency MEMS electrostatic vibration energy harvester with corona-charged vertical electrets and nonlinear stoppers *J. Phys.: Conf. Ser.* **660** 012003

[18] Basset P, Galayko D, Cottone F, Guillemet R, Blokhina E, Marty F and Bourouina T 2014 Electrostatic vibration energy harvester with combined effect of electrical nonlinearities and mechanical impact *J. Micromech. Microeng.* **24** 035001

[19] Galayko D, Dudka A, Karami A, O'Riordan E, Blokhina E, Feely O and Basset P 2015 Capacitive energy conversion with circuits implementing a rectangular charge-voltage cycle part 1: analysis of the electrical domain *IEEE Trans. Circuits Syst.* I **62** 2652–63

[20] Dorzhiev V, Karami A, Basset P, Marty F, Dragunov V and Galayko D 2015 Electret-free micromachined silicon electrostatic vibration energy harvester with the Bennet's Doubler as conditioning circuit *IEEE Electron Device Lett.* **36** 183–5

[21] Nayfeh A 2011 *Introduction to Perturbation Techniques* (New York: Wiley)

[22] Blokhina E, Galayko D, Basset P and Feely O 2013 Steady-state oscillations in resonant electrostatic vibration energy harvesters *IEEE Trans. Circuits Syst.* I **60** 875–84
[23] Senturia S D 2007 *Microsystem Design* (Berlin: Springer)
[24] Bao M and Yang H 2007 Squeeze film air damping in MEMS *Sensors Actuators* A **136** 3–27
[25] Pellegrini S P, Tolou N, Schenk M and Herder J L 2013 Bistable vibration energy harvesters: a review *J. Intell. Mater. Syst. Struct.* **24** 1303–12
[26] Harne R L and Wang K W 2013 A review of the recent research on vibration energy harvesting via bistable systems *Smart Mater. Struct.* **22** 023001
[27] Daqaq M F, Masana R, Erturk A and Quinn D D 2014 On the role of nonlinearities in vibratory energy harvesting: a critical review and discussion *Appl. Mech. Rev.* **66** 040801
[28] O'Riordan E, Dudka A, Galayko D, Basset P, Feely O and Blokhina E 2015 Capacitive energy conversion with circuits implementing a rectangular charge-voltage cycle, part 2: electromechanical and nonlinear analysis *IEEE Trans. Circuits Syst.* I **62** 2664–73
[29] Basset P, Blokhina E and Galayko D 2016 *Electrostatic Kinetic Energy Harvesters* (New York: Wiley)
[30] Basset P, Galayko D, Paracha A M, Marty F, Dudka A and Bourouina T 2009 A batch-fabricated and electret-free silicon electrostatic vibration energy harvester *J. Micromech. Microeng.* **19** 115025
[31] Truong B D, Le C P and Halvorsen E 2015 Experiments on power optimization for displacement-constrained operation of a vibration energy harvester *J. Phys.: Conf. Ser.* **660** 012012
[32] Meninger S, Mur-Miranda J O, Amirtharajah R, Chandrakasan A P and Lang J H 2001 Vibration-to-electric energy conversion *IEEE Trans. Very Large Scale Integr. Syst.* **9** 64–76
[33] Karami A, Basset P and Galayko D 2015 Electrostatic vibration energy harvester using an electret-charged mems transducer with an unstable auto-synchronous conditioning circuit *J. Phys.: Conf. Ser.* **660** 012025